Source Mechanism and Rupture Directivity of Small Earthquakes in the Changning Region, China, Using Dense Array Data

Youjie Jiang[1], Jiewen Zhang[1,2], Jinping Zi[1,2], and Hongfeng Yang[*1,2,3]

Abstract

Integrating focal mechanism solutions with rupture directivity analysis enables high-resolution characterization of subsurface fault geometry and earthquake rupture processes. However, resolving these parameters for small-magnitude earthquakes remains challenging due to small rupture sizes, short durations, and low signal-to-noise ratio. Here, we utilized a dense array of nodal seismometers in the Changning region, Sichuan basin, China, to study the focal mechanism and rupture directivity of aftershocks following the 2019 M_s 6.0 earthquake. Using PhaseNet+ and SKHASH, we first enhance the focal mechanism catalog ($1 < M_L < 4$). Then, applying the spectral ratio method with empirical Green's functions, we observe azimuth-dependent corner frequencies of two M_L~3 aftershocks by spectral fitting to the Brune's model, which are consistent with unilateral rupture. Our results reveal that the two earthquakes occurred at an unidentified conjugate fault and ruptured toward N60° E unilaterally, which significantly differs from the northwestward rupture of the M_s 6.0 mainshock. Furthermore, we obtain a rupture speed of approximately 0.6 times the shear-wave velocity. We also apply the spectral decomposition method to compute stress drops ($M_L > 1$), and their spatial variability reflects a long-term interplay between fluid injection and faults in the salt-mining area. These findings illuminate a complex fault system beneath the Changning anticline and highlight the importance of high-resolution seismic arrays in resolving rupture processes of small-magnitude events.

Cite this article as Jiang, Y., J. Zhang, J. Zi, and H. Yang (2026). Source Mechanism and Rupture Directivity of Small Earthquakes in the Changning Region, China, Using Dense Array Data, *Seismol. Res. Lett.* **XX**, 1–15, doi: 10.1785/0220250172.

Supplemental Material

Introduction

Determining source parameters of earthquakes, such as focal mechanisms, rupture directivity, and stress drop, is important in understanding subsurface fault structures, rupture kinematics and dynamics, and regional seismic hazard assessment. Focal mechanisms can be applied to illuminate the geometry of active faults and regional stress field orientations (e.g., Kisslinger, 1980; Zhang *et al.*, 2021), rupture directivity patterns reveal the dynamic evolution of fault systems and their influences on seismic energy distribution (e.g., Somerville *et al.*, 1997; Abercrombie *et al.*, 2017), and stress drops provide critical information about fault mechanics and energy radiation efficiency during rupture (e.g., Boatwright, 1978; Allmann and Shearer, 2007). The detailed earthquake source characterization is particularly crucial for induced seismicity, dominated by small-magnitude earthquakes while impacts profoundly in the operational safety of hydrocarbon and minerals production (Ellsworth, 2013; Yang *et al.*, 2017). The numerous aftershocks of intermediate and large induced earthquakes provide valuable opportunities to identify and characterize the spatial and temporal seismicity patterns and the source properties (e.g., Zi *et al.*, 2023). Such comprehensive analysis of aftershock sequences is essential for improving seismic hazard assessment and developing more effective risk mitigation strategies in industrial operations.

Intermediate and large earthquakes have the abundant low-frequency waveform information and good station coverage, benefiting for the source parameter determination. Reliable focal mechanisms for intermediate-to-large earthquakes can be obtained through broadband seismic waveform inversion methods such as Cut-and-Paste (CAP; Zhu and Helmberger, 1996) and ISOLated Asperities (Sokos and Zahradník, 2008). Meanwhile rupture directivity can be effectively characterized through azimuthal variations in source duration (Ni *et al.*, 2005) and wave amplitude (Tan and Helmberger, 2010).

1. Department of Earth and Environmental Sciences, The Chinese University of Hong Kong, Hong Kong, China, https://orcid.org/0009-0004-9446-2616 (YJ); https://orcid.org/0000-0001-8130-9453 (JZ); https://orcid.org/0000-0002-0891-8305 (JZ); https://orcid.org/0000-0002-5925-6487 (HY); 2. Shenzhen Research Institute, The Chinese University of Hong Kong, Shenzhen, China; 3. Institute of Environment, Energy and Sustainability, The Chinese University of Hong Kong, Hong Kong, China

*Corresponding author: hyang@cuhk.edu.hk

© Seismological Society of America

Downloaded from http://pubs.geoscienceworld.org/ssa/srl/article-pdf/doi/10.1785/0220250172/7723274/srl-2025172.1.pdf by Chinese University Hong Kong user on 07 April 202

However, determining source parameters for small-magnitude events is significantly challenging due to the higher frequency signals scattering by small-scale heterogeneities, limited azimuthal differences in ground-motion energy, and smaller rupture areas.

Previous studies have demonstrated that rupture characterization is a critical source feature across a wide range of earthquake magnitude (e.g., Chen *et al.*, 2021; Yang *et al.*, 2022; Tang *et al.*, 2024; Jia *et al.*, 2025; Lin *et al.*, 2025). Recent advances in seismic monitoring, particularly the deployment of dense seismic networks, have enabled more detailed studies of fault complexity (e.g., López-Comino and Cesca, 2018; Trugman *et al.*, 2021) and rupture directivity of small earthquakes (e.g., Folesky *et al.*, 2016; Király-Proag *et al.*, 2019). Focal mechanisms of small events can now be determined using first-motion polarity and *S*/*P* amplitude ratio methods (Hardebeck and Shearer, 2002, 2003). In the Sichuan basin, such methods reveal that the faulting mechanisms of induced earthquakes in the Weiyuan shale gas field are primarily dominated by reverse rupturing on preexisting north-northeast-trending faults, with a minority of normal-faulting events collocated with reverse faulting ones (Song *et al.*, 2025). The divergence in faulting styles indicates distinct structural controls or stress conditions, highlighting the critical role of focal mechanism determination of small earthquakes in understanding local fault complexity and stress heterogeneity. On the other hand, estimating the rupture directivity of small earthquakes primarily relies on analyzing the durations and spectra of body waves (e.g., Boore and Joyner, 1978; Warren and Shearer, 2006; Cesca and Heimann, 2011; Chen *et al.* 2021). Recently, using only one near-source strong-motion station, the polarization of *S* waves also can infer the rupture directivity of small earthquakes (Yao *et al.*, 2025). The combination of the focal mechanism inversion and directivity estimation can reduce nodal plane ambiguities for small events, especially for a complex fault network for which such ambiguities cannot be resolved by earthquake locations and focal mechanism solutions.

Here, we focus on the Changning region of the Sichuan basin where massive shale gas exploration and salt mining have been conducted (Fig. 1), accompanied by gradually larger earthquakes over time in recent years (Lei *et al.*, 2013, 2018). The June 2019 M_s 6.0 Changning earthquake, probably the largest induced event by industrial exploitation in the world to date (Liu and Zahradník, 2020), was followed by four $M_s > 5$ earthquakes and a series of aftershocks in neighboring regions, covering a span of approximately 20 km in space (Fig. 1a). Although the mainshock's source mechanism and directivity have been systematically investigated (e.g., Li *et al.*, 2020; Anyiam *et al.*, 2024), the aftershocks' rupture characteristics remain poorly constrained. If the focal mechanism and the rupture directivity were unaccounted for, it may cause biases in the measurement of earthquake source studies, such as stress drop, which are important for estimating seismic hazards and subsequent risk of industrial production near faults (Holmgren *et al.*, 2019; Yu *et al.*, 2022; Zhang *et al.*, 2024).

In this study, utilizing a dense array with wide azimuthal coverage in the Changning region, we first compile an enhanced focal mechanism catalog by constraining small-earthquake ($M_L > 1$) focal mechanisms with first-motion polarity measurements, and then determine the rupture directivity for two small earthquakes ($M_L \sim 3$) in detail. Applying the state-of-the-art PhaseNet+ (Zhu *et al.*, 2025) and SKHASH (Skoumal *et al.*, 2024), we obtain 857 high-quality solutions of focal mechanisms. Using the multiple spectral ratio method to observe the difference of azimuth-dependent corner frequencies, we investigate the rupture processes of the two small-size aftershocks (M_L 3.3 and 3.2, respectively), including rupture direction, rupture speed, and stress drop. We obtain stress drops for 1183 earthquakes ($M_L > 1$) using the spectral decomposition method, and analyze the spatial distribution in the salt-mining area. These findings illuminate a complex interlocked fault system beneath the Changning anticline and highlight the importance of high-resolution seismic arrays in resolving small-magnitude earthquake rupture processes. Our results also motivate the importance of evaluating the focal mechanism and rupture directivity on the probabilistic seismic hazard and risk assessment in Changning.

Geological Setting and Data

Geological setting

The Sichuan basin, situated as the most stable tectonic unit within the Yangtze craton, is bounded to the west by the Sichuan-Yunnan block. Although historical seismic activity has concentrated along its northwestern and southwestern boundaries where basement faults intersect the Longmenshan and Xianshuihe-Xiaojiang fault systems, the interior of the basin remained seismically inactive until the surging of recent industrial operations in the southern part. Since 2010, the activities of shale gas exploration and salt-mining solution (dating back to the 1970s) have triggered several earthquakes with $M_L > 4$ and shallow depths (3–5 km), such as the 2019 M_L 4.9 Rongxian earthquake (Yang *et al.*, 2020) and the 2021 M_s 6.0 Luzhou earthquake (Zhao, Jiang, *et al.*, 2023). In the Weiyuan shale gas field, a detailed analysis of the 2019 M_L 5.6 earthquake sequence revealed 11 months of precursory fault activation directly linked to hydraulic fracturing operations (Zi *et al.*, 2025). The Changning region, particularly the Changning salt-mining area, has experienced a significant increase in seismicity rate. The M_s 6.0 Changning earthquake, which occurred on 17 June 2019, is the largest event in this region, leading to 13 fatalities and 299 residents injured with a total economic loss of 56.17 billion in RMB.

Our study focuses on the salt-mining area in the north of the Changning region, located in the Changning-Shuanghe anticline (Fig. 1b in red part). The southeast-extending asymmetric anticline features a steep northeast wing with northwest-striking

Downloaded from http://pubs.geoscienceworld.org/ssa/srl/article-pdf/doi/10.1785/0220250172/7723274/srl-2025172.1.pdf by Chinese University Hong Kong user on 07 April 202

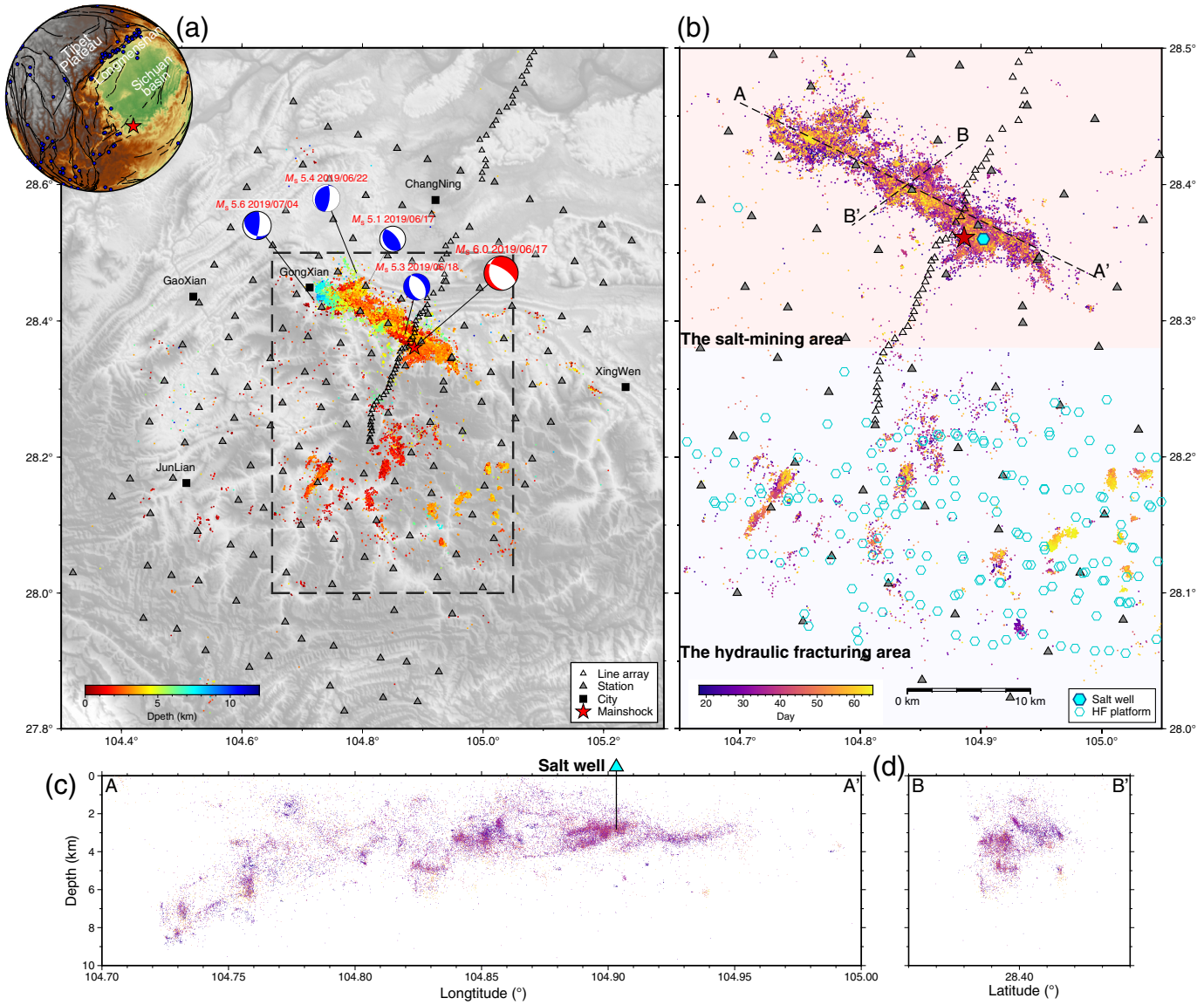


Figure 1. (a) Relocated seismicity using utilized dense array in Changning region. Focal mechanism plots (Anyiam *et al.*, 2023) represent focal mechanisms of the $M_s > 5$ Changning earthquake sequence. The inset shows locations of historical (1972–2015) $M_L > 5$ earthquakes in blue dots (see Data and Resources) in and around the Sichuan basin. (b) Zoomed in the view of the dashed box in panel (a). (c,d) Cross-section views of aftershocks for A–A′ and B–B′ in panel (b). HF, hydraulic fracturing. The color version of this figure is available only in the electronic edition.

faults of different dip angles, and a gentler southwest wing connecting to the wide and flat Luochang syncline (Fig. 1c). The M_s 6.0 mainshock occurred in the salt-mining area, and an extensive aftershock sequence depicts a complex multifault network of the anticlinal system, which is composed of numerous normal, reverse, and strike-slip faults. Previous research (Li *et al.*, 2020) demonstrated the mainshock is mainly a strike-slip earthquake, and both the centroid and hypocentral depths are shallow (~4 km) using the CAP method, with a unilateral rupture propagating northwestward for about 14 km. Using a local and regional waveform data set, Anyiam *et al.* (2024) also determined and synthetically validated the focal mechanism solutions of the $M_s > 5$ Changning sequence and 30 $M_s > 2$ aftershocks, as well as inferred excessive pore pressures within the source zone. The aftershocks may be closely related to increased pore pressures on the seismogenic faults due to decades-long fluid injection and migration. Li *et al.* (2023) and Anyiam *et al.* (2023) suggest the seismicity is distributed close to the target shale formations in depth and along high-seismic velocity boundaries in the hydraulic fracturing area. On the other hand, seismicity in the salt-mining area of the Changning region is found mostly in areas characterized by high-V_S anomaly in the basement (Zuo *et al.*, 2020; Liu *et al.*, 2023), suggesting locally high-seismic velocity and low permeability.

Dense array

The dense array used in this study was deployed by the Geophysical Exploration Center of the China Earthquake

Downloaded from http://pubs.geoscienceworld.org/ssa/srl/article-pdf/doi/10.1785/0220250172/7723274/srl-2025172.1.pdf by Chinese University Hong Kong user on 07 April 202

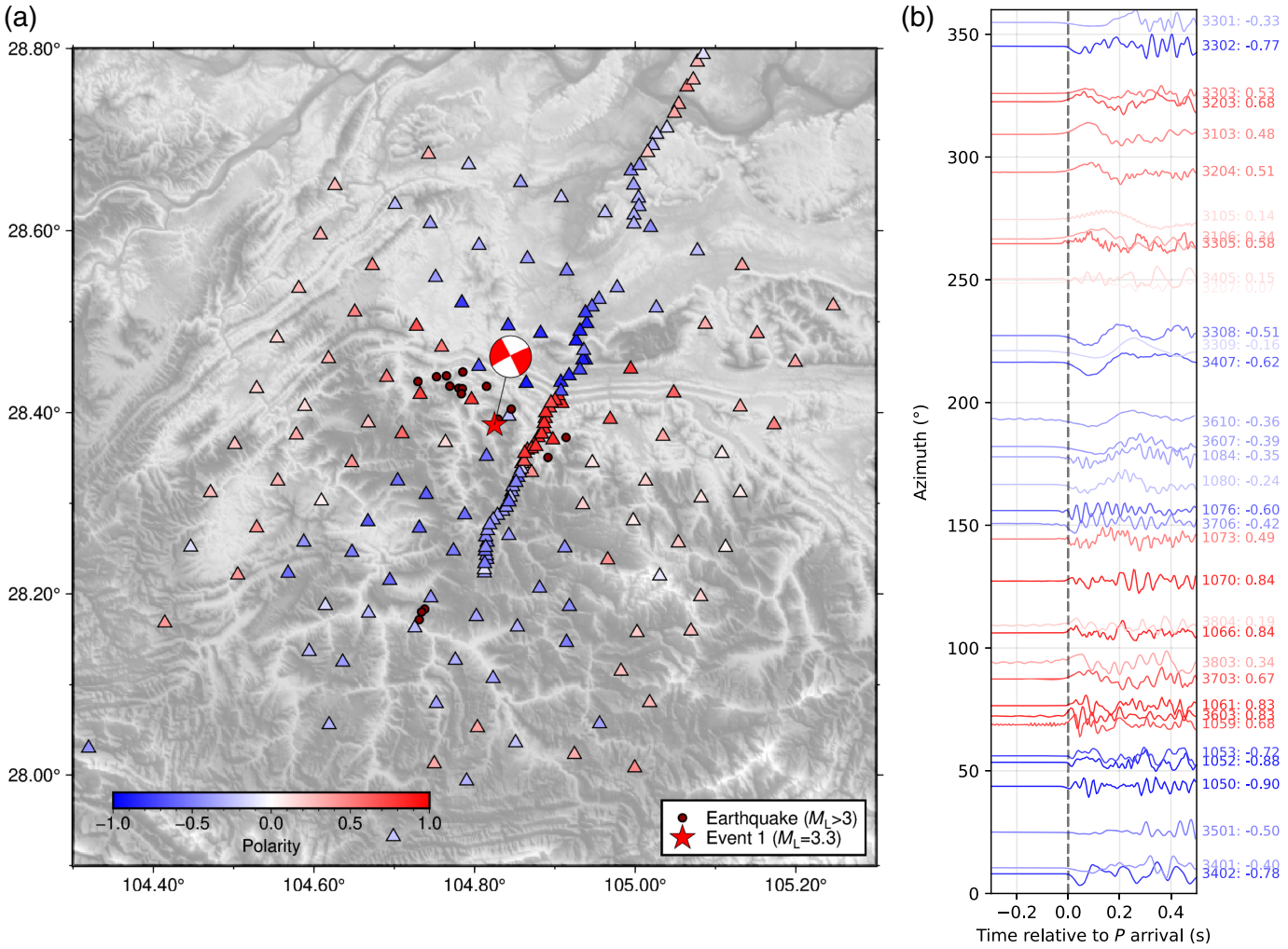


Figure 2. (a) Focal mechanism inversion of event 1 using *P*-wave polarities. (b) Waveforms within the 0.8 s window (0.3 s before the *P* arrival and 0.5 s after). The dashed line represents the predicted *P* arrivals for event 1. Red and blue indicate positive and negative first-motion polarity prediction as panel (a), followed by the station name and the probability or the confidence. The color version of this figure is available only in the electronic edition.

Administration (CEA). It consists of 298 short-period, three-component portable seismometers with two sampling rates of 100 and 200 Hz, starting from 6 July to 21 August 2019 in the Changning area. The seismic monitoring system consists of a square array comprising 153 stations distributed across a 60 km × 50 km region, and a linear array of 145 stations in the ranges of 27.8°–28.8° N and 104.3°–105.2° E. We only choose the stations with a sampling rate of 200 Hz (Fig. 1a) for analysis. The wide azimuthal coverage is expected to provide better resolution of small-magnitude events and their source characteristics.

Methods

Focal mechanism inversion

The robust foundation of our analysis is based on the relocated earthquake catalog (Zhao, Zhang, *et al.*, 2023), which identified events ranging from M_L − 0.5 to 3.9 using the same dense array data set, with 14 larger events reaching up to M_L 3.0. Because of the signal-to-noise ratio (SNR) of data, we here focus on events with $M_L > 1$. Based on the previous phase arrival time of the earthquake catalog, we use PhaseNet+, a multitask deep learning model built upon PhaseNet (Zhu and Beroza, 2019), to simultaneously predict phase arrivals and onset polarities. The predicted polarity ranges between −1 and 1 representing the probability of downward (negative) or upward (positive) onset. For example, the azimuthal *P*-wave polarity pattern of event 1 (2019071410171814) reveals a left-lateral strike-slip focal mechanism (Fig. 2). Stations in the northeast and southwest quadrants, such as 3302 (azimuth 345°) and 3808 (azimuth 162°), exhibit dominant negative polarities, consistent with compressional quadrant radiation predicted by the strike-slip focal mechanism. Conversely, northwest and southeast quadrant stations, for instance, 1059 (azimuth 69°) and 3204 (azimuth 294°) display positive polarities, aligning with dilatational quadrant expectations.

Downloaded from http://pubs.geoscienceworld.org/ssa/srl/article-pdf/doi/10.1785/0220250172/7723274/srl-2025172.1.pdf by Chinese University Hong Kong user on 07 April 202

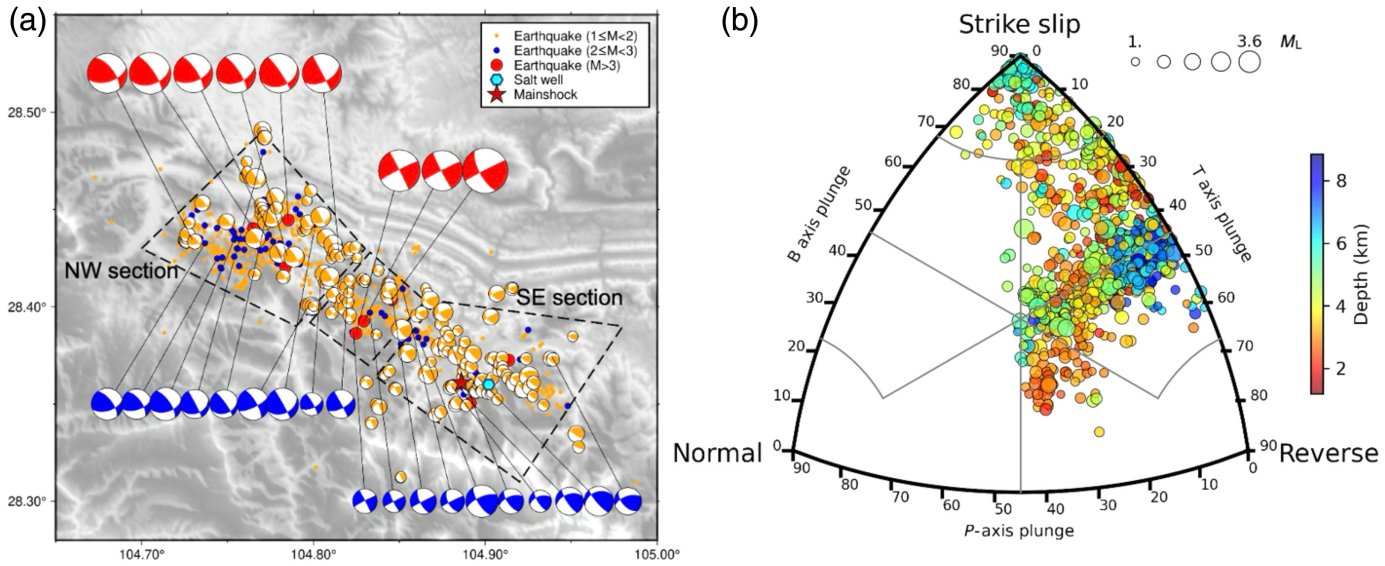


Figure 3. (a) Focal mechanisms of earthquakes ($M_L > 1$) in the salt-mining area using SKHASH. (b) Faulting types of focal mechanisms determined from panel (a). The color version of this figure is available only in the electronic edition.

To resolve the fault geometry and kinematics of the analyzed events ($M_L > 1$), we determined earthquake source mechanisms using SKHASH, largely based on the HASH algorithm (Hardebeck and Shearer, 2003). The wide coverage of our seismic network enabled us directly to utilize the predicted *P*-wave polarities as input data from multiple stations across diverse azimuths. The minimum number of required polarities is 8, within a maximum azimuthal gap of 90°. SKHASH implements a rigorous quality assessment framework for focal mechanism solutions through systematic misfit quantification. Solutions are assigned quality grades from "A" to "D," based on nodal plane constraint criteria, for which grade A requires the probability that the focal mechanism solution should be larger than 0.8 (Fig. S1, available in the supplemental material to this article).

Rupture direction

To determine their fault planes, we estimate the rupture directivities of two relatively large events ($M_L \sim 3$), 2019071410171814 (event 1) and 2019072208190033 (event 2), which occurred in the central section of the Changning anticline (Figs. 3 and 4). Rupture directivity can clarify faulting systems and the regional stress environment, especially for complex fault networks with multiple active fault strands.

Assuming an omega-square source model (Aki, 1967), the displacement spectrum exhibits an azimuth-dependent corner frequency that is inversely proportional to the source duration. To identify the corner frequency of target events, we apply the empirical Green's function (EGF) technique that uses the waveforms of closely located smaller events as a reference to remove common path and site effects from a target event. To mitigate the influence of biased frequency contents from *S* waves or coda using a time window with a fixed length, we exclusively analyze spectrum between *P*- and *S*-wave arrivals (e.g., Fig. 5c). Furthermore, we set a cross-correlation coefficient threshold of 0.7 for the band-pass filtered waveforms inside 1–10 Hz (e.g., Fig. 5d). The selected EGFs have focal mechanisms similar to the main event and are at least one magnitude unit smaller (Fig. 5a), satisfying the EGF criteria (Abercrombie, 2015; Abercrombie *et al.*, 2017). Because of the limitation of instrument response, we exclude frequency contents outside 1–80 Hz range. To mitigate the influence of noise, we apply strict criteria to screen out noisy waveforms: for each spectrum, 90% of the frequency sampling points between 1 and 80 Hz shall have an SNR larger than 3, with the noise spectrum calculated in a 1 s window before the *P*-wave arrival, following the criteria as Zhang *et al.* (2024). The *P*-wave window starts 0.1 s before the direct *P*-wave arrival and lasts to the *S*-wave arrival. Before calculating the spectrum, we use a multitaper method (Python package: spectrum, pmtm function) to get more stable spectral results.

The target events are events 1 and 2, which occurred in the center of the Changning anticline and showed different nodal plane patterns compared with those on the two sides of the anticline (Fig. 3a). The two events are found to have 45 and 69 EGFs, respectively. Then, the corner frequency of the mainshock at different stations can be obtained by fitting the spectral ratio from the Brune spectral model (Brune, 1970) to the spectral ratio of the target and EGF events (e.g., Abercrombie, 2014; Huang *et al.*, 2016):

$$\frac{u_1(f)}{u_2(f)} = \frac{M_1}{M_2}\frac{1+\left(\frac{f}{f_{c2}}\right)^2}{1+\left(\frac{f}{f_{c1}}\right)^2}, \quad (1)$$

in which M_1 is the seismic moment of the target event, f_{c1} is the corner frequency of the target event, M_2 is the seismic

Downloaded from http://pubs.geoscienceworld.org/ssa/srl/article-pdf/doi/10.1785/0220250172/7723274/srl-2025172.1.pdf by Chinese University Hong Kong user on 07 April 202

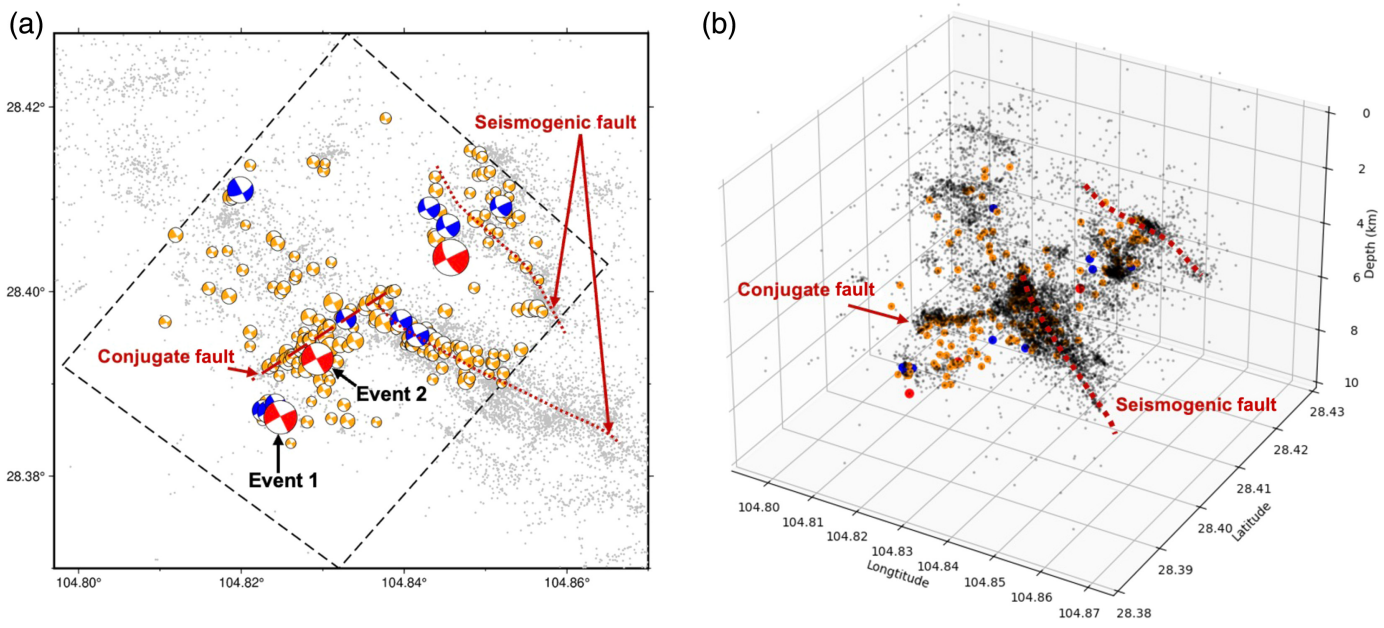


Figure 4. Focal mechanisms of earthquakes in the center section of the Changning-anticline fault system, and inferred fault architecture from seismicity, in (a) horizontal map and (b) 3D. The inferred faults as shown by red-dashed lines align well with the aftershock locations (gray dots). The colors of focal mechanism plots are the same as in Figure 3. The color version of this figure is available only in the electronic edition.

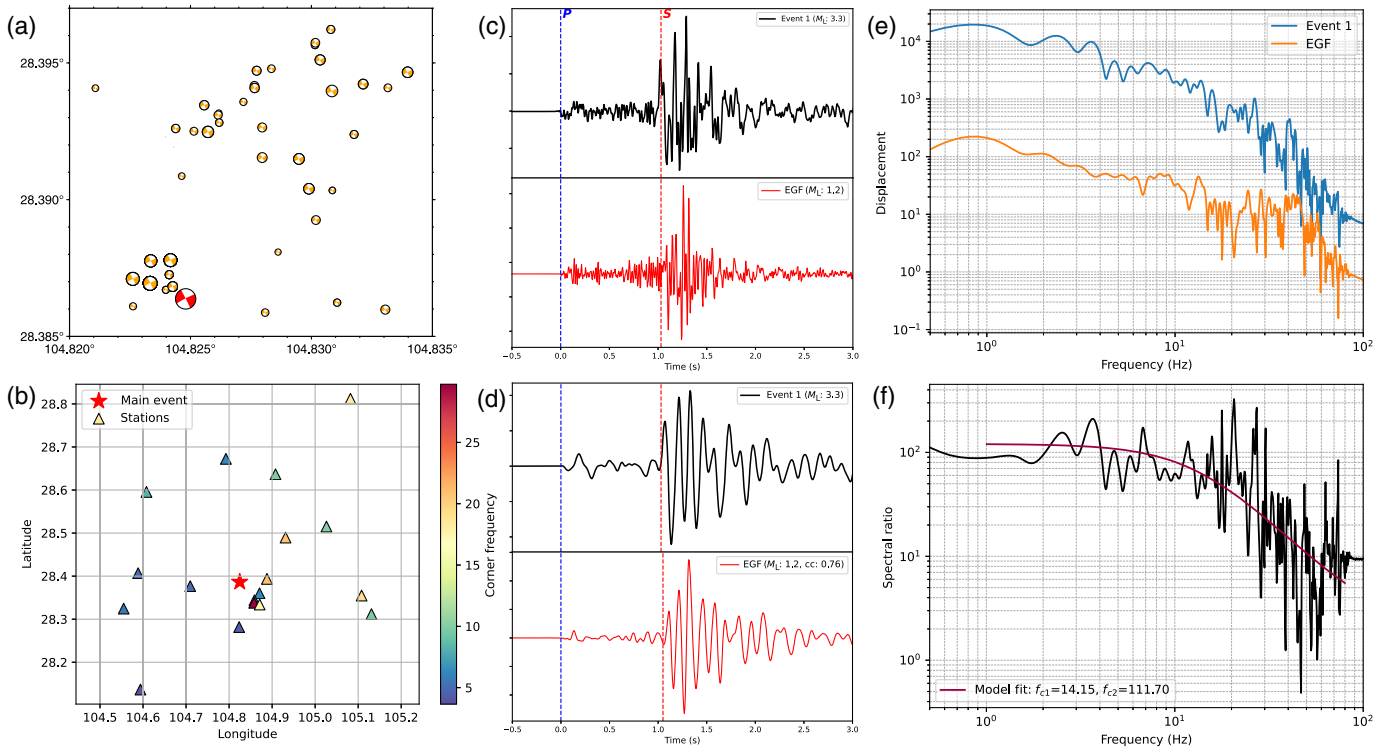


Figure 5. (a) A map shows the locations and focal mechanisms of event 1 (red) and its empirical Green's functions (EGFs; yellow). (b,c,e,f) One pair with event 1 and its EGF. (b) Raw vertical-component waveform. (d) Spatial distribution of corner frequency at different stations. (e) Normalized filtered waveform (1–10 Hz). (c,f) *P*-wave displacement spectra and the spectral ratio of this pair. The color version of this figure is available only in the electronic edition.

Downloaded from http://pubs.geoscienceworld.org/ssa/srl/article-pdf/doi/10.1785/0220250172/7723274/srl-2025172.1.pdf by Chinese University Hong Kong user on 07 April 202

moment of the EGF event, f_{c2} is the corner frequency of the EGF event.

The shape of the spectral ratios computed from different EGF events reflects the characteristics of the source spectrum for the target event. To improve the accuracy of the source spectrum, we perform multiple spectral ratio analysis, stacking spectral ratios from at least three high-quality EGF pairs per station. The analysis has been designed to prioritize the appropriateness of the EGF event selection, and its stability by stacking the best EGF events.

Many previous studies have characterized rupture directivity patterns as unilateral, bilateral, or complex (e.g., Abercrombie *et al.*, 2017; Chu *et al.*, 2024). To quantify the directivities of two target events, we analyze the azimuthal pattern of corner frequency, which is inversely proportional to the apparent pulse duration. A unilateral rupture earthquake produces higher corner frequency and shorter pulse durations in the direction of rupture propagation. For a unilateral rupture, the apparent pulse duration δt can be written as

$$\delta t = t_0 - \frac{\Delta \cos(\theta)}{c} = t_0 + \Delta\Gamma, \tag{2}$$

$$\Gamma = \frac{-\cos(\theta)}{c}, \tag{3}$$

in which t_0 and Δ are the true time difference and rupture distance, respectively. θ is the azimuth of the station relative to the rupture direction, c is the considered phase velocity (P wave in our study) near the source, and Γ is the directivity parameter.

Rupture speed

The good azimuthal coverage of the dense array also enables simultaneous resolution of fault geometry, rupture length, and rupture speed. Rupture velocity is a key source parameter to describe the dynamic property of seismic source. Assuming unilateral directivity in a horizontal plane (e.g., Boatwright, 2007), the directivity coefficient through the corner frequency ratio is

$$Cd(\theta) = \frac{f_c}{f_a}, \tag{4}$$

$$Cd(\theta) = \frac{1}{1 - (\frac{V_r}{V_s})\cos(\theta - \theta_0)}, \tag{5}$$

in which f_a is the apparent corner frequency, f_c is the true corner frequency as a function of azimuth (θ), V_r and V_s are the rupture velocity and shear-wave speed, respectively, θ is the station azimuth, and θ_0 is the rupture direction.

Based on the aforementioned rupture direction method, we can get the rupture direction θ_0 and the apparent corner frequency. Combining with equations (4) and (5), it is possible for us to obtain the best fitting of the ratio of the rupture velocity and shear-wave speed.

Stress-drop estimation

Using the spectral ratio method, we can only estimate stress drops for relatively large events ($M_L \sim 3$), because the EGFs are at least one magnitude unit smaller than the main event (Abercrombie *et al.*, 2017). To estimate stress drops for more small earthquakes, we apply an improved spectral decomposition method (Zhang *et al.*, 2024, Zhang and Yang, 2025). Using a global-optimization algorithm, the differential evolution (DE; Storn and Price, 1997), this new approach reduces the uncertainty of the corner frequency estimation and finds the optimized combination of stress drops in all the magnitude bins. The observed spectra can be analyzed as the convolution of an event term, a path term, and a site term. More specifically, for earthquakes recorded by at least three stations, we use the spectral decomposition method to solve for their event spectra (Shearer *et al.*, 2006), and obtain a correction term, the empirical correction spectrum (ECS), using the DE method to isolate the source spectra from the event spectra. Then, the earthquake corner frequencies are estimated by fitting the source spectra to the Brune's source spectrum model:

$$u(f) = \frac{\Omega_0}{1 + \left(\frac{f}{f_c}\right)^2}, \tag{6}$$

in which $u(f)$ is the source spectrum, Ω_0 is the zero-frequency spectral level (proportional to log M_0), and f_c is the corner frequency.

We obtain 1475 reliable P-wave event spectra from the 1989 recorded events ($1 < M_L < 4$). To obtain the moment magnitudes of these earthquakes, we follow the magnitude calibration workflow as Shearer *et al.* (2006), Zhang, Chen, and Abercrombie (2022), and Vandevert *et al.* (2024), to establish a conversion relationship from local magnitude to moment magnitude, utilizing the average amplitude in the low-frequency plateau of the event spectra. We average the event spectra within bins of 0.2 units in local magnitude. There are only 7, 3, 3 spectra contributing to the bin 11, 12, and 13, separately, compared to 155 for $M_L = 1.6 - 1.8$ and 222 for $M_L = 1.4 - 1.6$ (Fig. S2b). The bins with few data (<10 events) have irregular shaped spectra compared with other bins stacking a larger number of spectra. To improve the estimation of ECS (Shearer *et al.*, 2006, 2019), we use the $M_L = 1.0$–3.0 results to calculate the final ECS (Fig. S10), and then correct their event spectra ($M_L > 1$).

We compute the median estimated log M_0 for M_L bins of width 0.2 magnitude to better fit the line (Fig. 6). We convert the relative log moments to absolute moment estimates (M_0) and their corresponding M_w estimates (Hanks and Kanamori, 1979). Based on the scaling of the log M_0 and the local magnitude for P waves, the linear relationship of M_L and M_w in the study region is

$$\begin{cases} M_w = 0.68 \times M_L + 0.96, & 1 < M_L < 3 \\ M_w = 0.84 \times M_L + 0.48, & M_L > 3 \end{cases}. \tag{7}$$

Downloaded from http://pubs.geoscienceworld.org/ssa/srl/article-pdf/doi/10.1785/0220250172/7723274/srl-2025172.1.pdf by Chinese University Hong Kong user on 07 April 202

From the estimated f_c and M_0 values, we estimate Brune stress drops (Brune, 1970) as,

$$\Delta\sigma = \frac{7}{16}\left(\frac{M_0}{r^3}\right) = \frac{7}{16}M_0\left(\frac{f_c}{kV_S}\right)^3, \quad (8)$$

$$f_c = k\frac{V_S}{r}, \quad (9)$$

in which V_S represents shear velocity, M_0 is the seismic moment of the earthquake, k is a constant depending on model assumptions, and r stands for source radius.

For the shear velocity, we use the tomography results of the Changning region from Li *et al.* (2023; Fig. S3). The average 1D velocity model correlates with low V_S in shallow crust. Beneath the Changning anticlinal system, the Cambrian to Silurian caprocks overlying the Sinian Dengying Formation are target layers for salt extraction (Jia *et al.*, 2006; Anyiam *et al.*, 2024). Specially, the Dengying Formation, an overlying quartz- and silica-rich slip-prone caprock, is between 2.7 and 3 km depth (Sun *et al.*, 2017; Lei *et al.*, 2019).

Results

Because of the dense array's wide azimuth coverage, we achieve robust solutions only using *P*-wave polarities, resulting in a lower uncertainty (Fig. S1). The resulting focal mechanism catalog has 1792 solutions of varying qualities, accounting for ~87% of earthquakes ($M_L > 1$) from the hypocenter catalog. We focus on 857 focal mechanisms associated with the highest quality "A" (Fig. 3a). In particular, the "A" quality focal mechanisms have a larger number of polarity picks (≥24), lower fault-plane uncertainties (<30°), higher probabilities (>80%), and lower polarity misfits (<15%; Fig. S4).

Based on the selected high-quality focal mechanisms, we further identify the principal axes (P, B, and T) to characterize the potential faulting types according to the Kaverina projection (Álvarez-Gómez, 2019). Our results reveal the compressional types of faulting, including strike slip (39%), strike-slip-reverse (33%), and reverse-strike-slip (19%; Fig. 3b). There patterns are consistent with both aftershock focal mechanisms in the salt-mining region (Yi *et al.*, 2020) and the regional tectonic background. The prevailing orientation of maximum-horizontal principal stress (SH_{max}) falls within the range between N30° E and N70° E on the Changning anticline (Liu *et al.*, 2021), which aligns with the P-axis orientations from the focal mechanism solutions. The predominant faulting type for the central section is pure strike slip, compared with reverse and reverse-strike-slip types dominant in the northwest and southeast sections (Fig. S5).

The fitting results of the two target events, located in the center section, demonstrates a cosine relationship of azimuth-dependent corner frequencies varying across different azimuths, showing clear unilateral rupture directivity. Consequently, the minimum $1/f_c$ is the rupture direction: 65° for event 1 (Fig. 7), 59° for event 2 (Fig. 8). For event 1, the corner frequency is ~16.67 Hz in the forward direction and ~4.55 Hz in the backward direction (Fig. 7a). The apparent corner frequency is 7.14 Hz, smaller than the geometric mean (9.52 Hz) and the median (8.91 Hz). For event 2, the apparent corner frequency is 5.88 Hz (Fig. 8a). The northeast rupture directions (65° for event 1, 59° for event 2) align with one of the focal mechanism nodal planes but notably differ from the mainshock's northwestward rupture direction. Based on the detailed analysis of the rupture directions and the apparent corner frequencies, we obtain the best fitting of the ratio of the rupture velocity and shear velocity ($V_r/V_s = 0.64$) for event 1, when the shear velocity is 3.2 km/s (Fig. 7e). Meanwhile, for event 2, $V_r/V_s = 0.59$ (Fig. 8e).

For equation (8), assuming an asymmetrical circular source, k = 0.21 for P wave when $V_r/V_s = 0.6$ (Kaneko and Shearer,

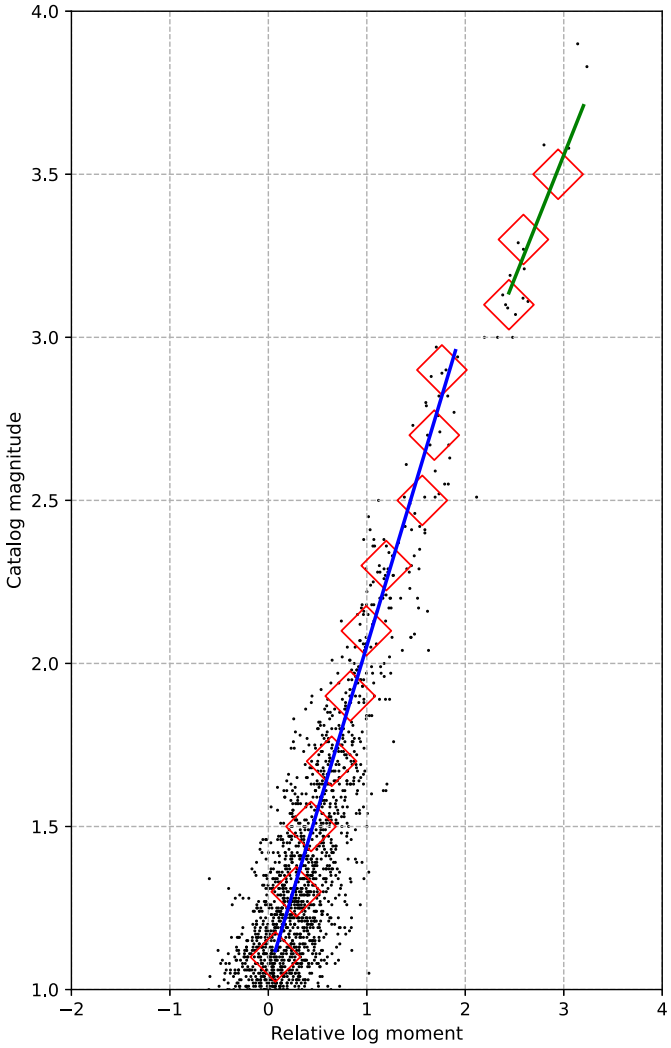


Figure 6. Catalog magnitude (M_L) versus relative log moment, binned in increments of 0.2 in M_L (red square), and the best-fitting lines to the resulting bins are shown for $1 < M_L < 3$ (in blue) and $M_L > 3$ (in green). The color version of this figure is available only in the electronic edition.

Downloaded from http://pubs.geoscienceworld.org/ssa/srl/article-pdf/doi/10.1785/0220250172/7723274/srl-2025172.1.pdf by Chinese University Hong Kong user on 07 April 202

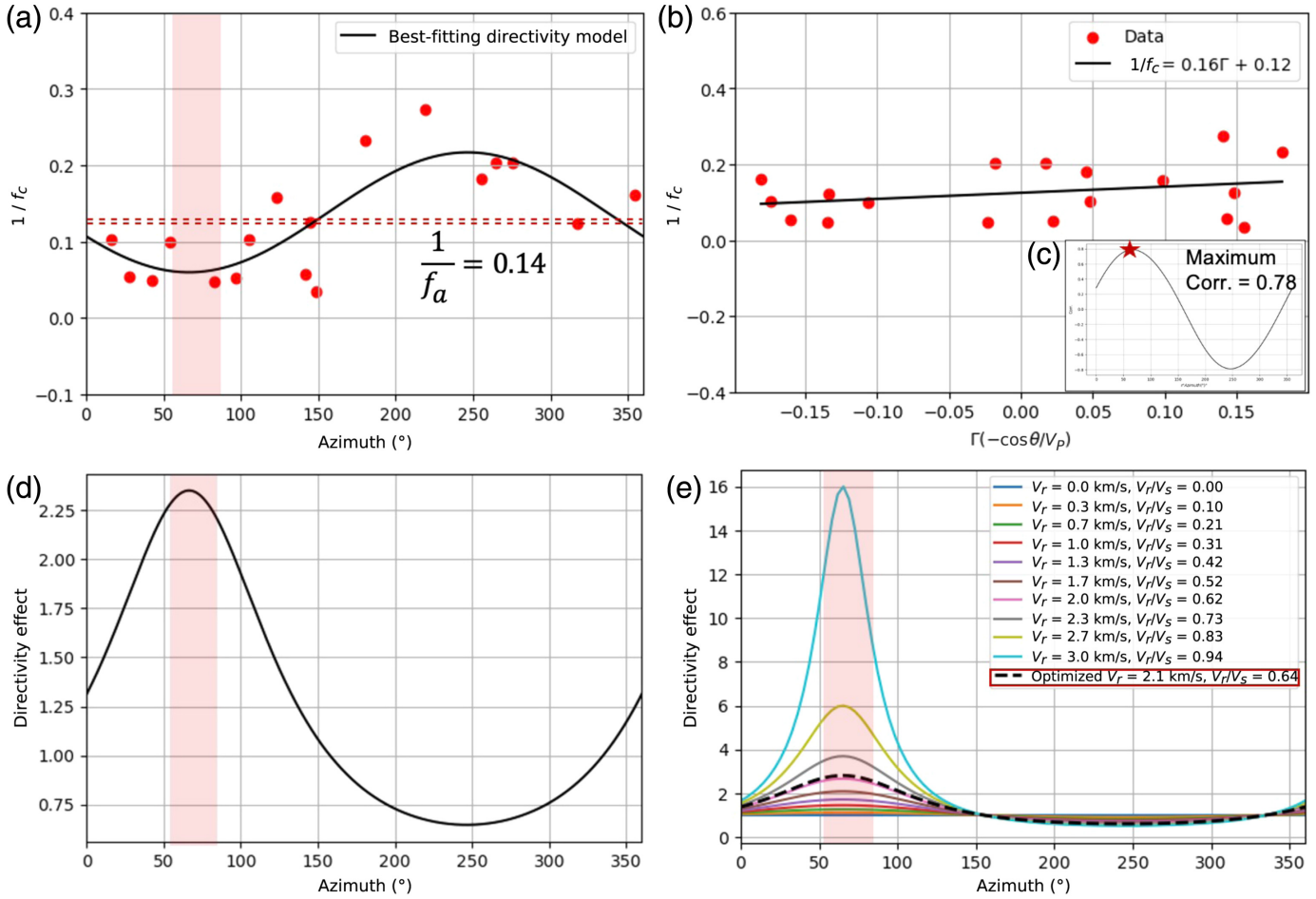


Figure 7. Source parameter analysis of event 1. The black-solid lines in panels (a) and (b) show the best-fitting directivity model. (c) Correlation coefficient (Corr.) as a function of possible azimuths, with the optimal rupture direction marked by a star. (d) Directivity effect of event 1. The dashed lines in panel (e) shows the best-fitting rupture speed verse the shear velocity. The color version of this figure is available only in the electronic edition.

2015). Here, we use the apparent corner frequency obtained from the fitting result and the shear velocity from Li *et al.* (2023). The stress drops are 29 MPa for event 1 and 12 MPa for event 2. In addition, in spectral decomposition method, we use $k = 0.38$ for the *P*-wave results (Kaneko and Shearer, 2015) and the same shear velocity model (Li *et al.*, 2023) to estimate stress drop. We obtain stress drops for a total of 631 events ($M_L > 1$) within the salt-mining area (Fig. 9). The median and geometric mean of stress drops are 7.91 and 8.83 MPa, respectively. We determine that the center section displays elevated median stress drops ($\Delta\sigma = 9.36$ MPa) compared to the northeastern and southwestern sections ($\Delta\sigma = 6.13$ and 8.90 MPa, respectively; Fig. 9 and Fig. S6b). The stress drops are observed significantly increasing in the depth range of 2–4 km, but their depth dependence disappears below 6 km (Fig. 9c). Meanwhile, the stress drops are found not visibly scaled with moment magnitudes (Fig. 9d), supporting the self-similarity assumption (Aki, 1967). A few of the smallest events deviate from this trend due to the estimated corner frequencies outside the frequency band.

Discussion

Uncertainty of small-earthquake focal mechanisms and rupture directivities

The SKHASH algorithm uses a grid-search approach that identifies a set of acceptable focal mechanism solutions (Skoumal *et al.*, 2024). In our study, we set the fraction of assumed bad polarities at 0.1. The acceptable solutions are defined as those with a *P*-wave polarity misfit below this threshold. SKHASH then determines the best-fit focal mechanism by averaging these acceptable solutions, given the possible source depth and velocity model. The quality rankings of the focal mechanism are based on the statistical tightness of the acceptable solution set and the number of polarity misfits for the preferred solution. Meanwhile, the uncertainty is determined by the observed polarities and computed takeoff angles, as well as the root mean square difference from the preferred solution and acceptable solutions.

The uncertainty in focal mechanism solutions for small earthquakes is influenced mainly by the quantity of *P*-wave polarities and the station distribution (Yang *et al.*, 2012). The reliability of PhaseNet+ polarity identification has been

Downloaded from http://pubs.geoscienceworld.org/ssa/srl/article-pdf/doi/10.1785/0220250172/7723274/srl-2025172.1.pdf by Chinese University Hong Kong user on 07 April 202

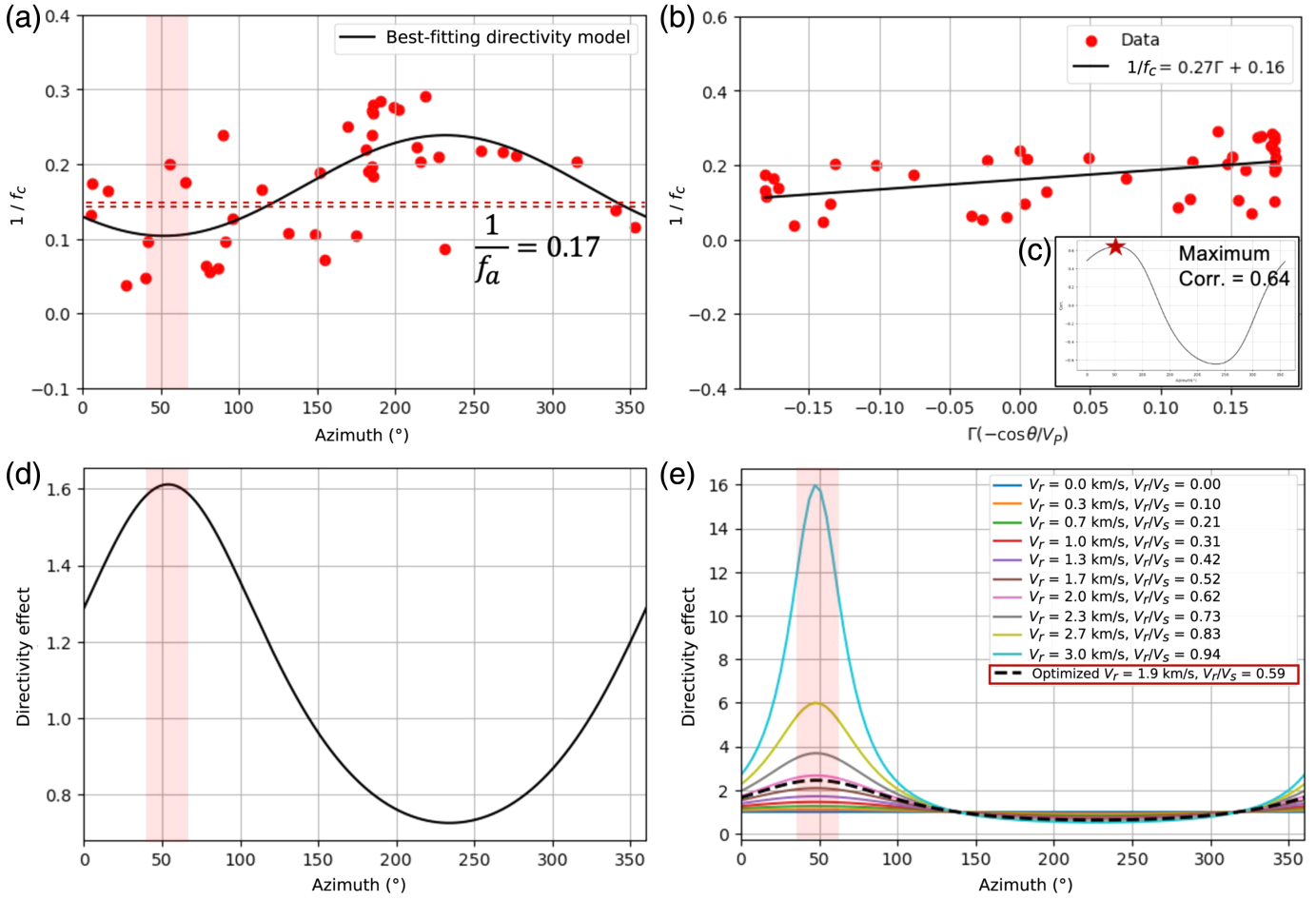


Figure 8. Source parameter analysis of event 2. The black-solid lines in panels (a) and (b) show the best-fitting directivity model. (c) Correlation coefficient (Corr.) as a function of possible azimuths, with the optimal rupture direction marked by a star. (d) Directivity effect of event 2. The dashed lines in panel (e) show the best-fitting rupture speed verse the shear velocity. The color version of this figure is available only in the electronic edition.

examined by Song *et al.* (2025). Because of the wide station coverage, we achieve reliable solutions only using *P*-wave polarity, including a lower uncertainty (Fig. S1). Notably, the nodal plane uncertainty of all qualities focal mechanisms correlates with the focal mechanism probability (Fig. S4c) and the polarity misfit (Fig. S4d). Such trends with the magnitude (Fig. S4a) and the number of polarities (Fig. S4b) are less obvious. It remains challenging to derive reliable focal mechanism solutions for smaller earthquakes ($M_L < 1.5$) given the station coverage. Therefore, in this study we only account for the good quality "A" because our results to mitigate the impact of uncertainty in focal mechanism inversion. The "A" quality focal mechanism solutions show consistency with the regional stress field observations (Zhang, Liang, *et al.*, 2022) in the three distinct seismotectonic subregions.

Station coverage is the primary reason that affects our analysis of rupture directivity. We apply a bootstrap analysis, performing 1000 bootstrap iterations to evaluate the rupture azimuth uncertainty. It reveals that rupture azimuth uncertainties exceed 10° with fewer than 12 recording stations for event 1 (Fig. S7) and 18 stations for event 2 (Fig. S8). The rupture directivity estimates align with one of the nodal planes (e.g., Fig. S9), confirming the robustness of the resolved focal mechanism solution and rupture direction.

Analysis of stress-drop estimation

The stress drops for events 1 and 2, determined as 29 and 12 MPa, respectively, using the spectral ratio method, are significantly higher than the median stress drop of 9.36 MPa estimated for the central Changning anticline segment using the spectral decomposition method. However, due to the lack of events for $M_L > 3$, which could result in unreliable stress-drop estimates in this magnitude range (Fig. S2), we prefer to compare the corner frequency results rather than the absolute stress-drop values. The corner frequencies obtained from the spectral decomposition method are 9.31 and 8.94 Hz for events 1 and 2, higher than the apparent corner frequencies considering rupture directivity using the spectral ratio method (Table S1). Specifically, for event 1, which shows a better fit in the rupture direction analysis, the corner frequency from the spectral decomposition method aligns more closely with

Downloaded from http://pubs.geoscienceworld.org/ssa/srl/article-pdf/doi/10.1785/0220250172/7723274/srl-2025172.1.pdf by Chinese University Hong Kong user on 07 April 202

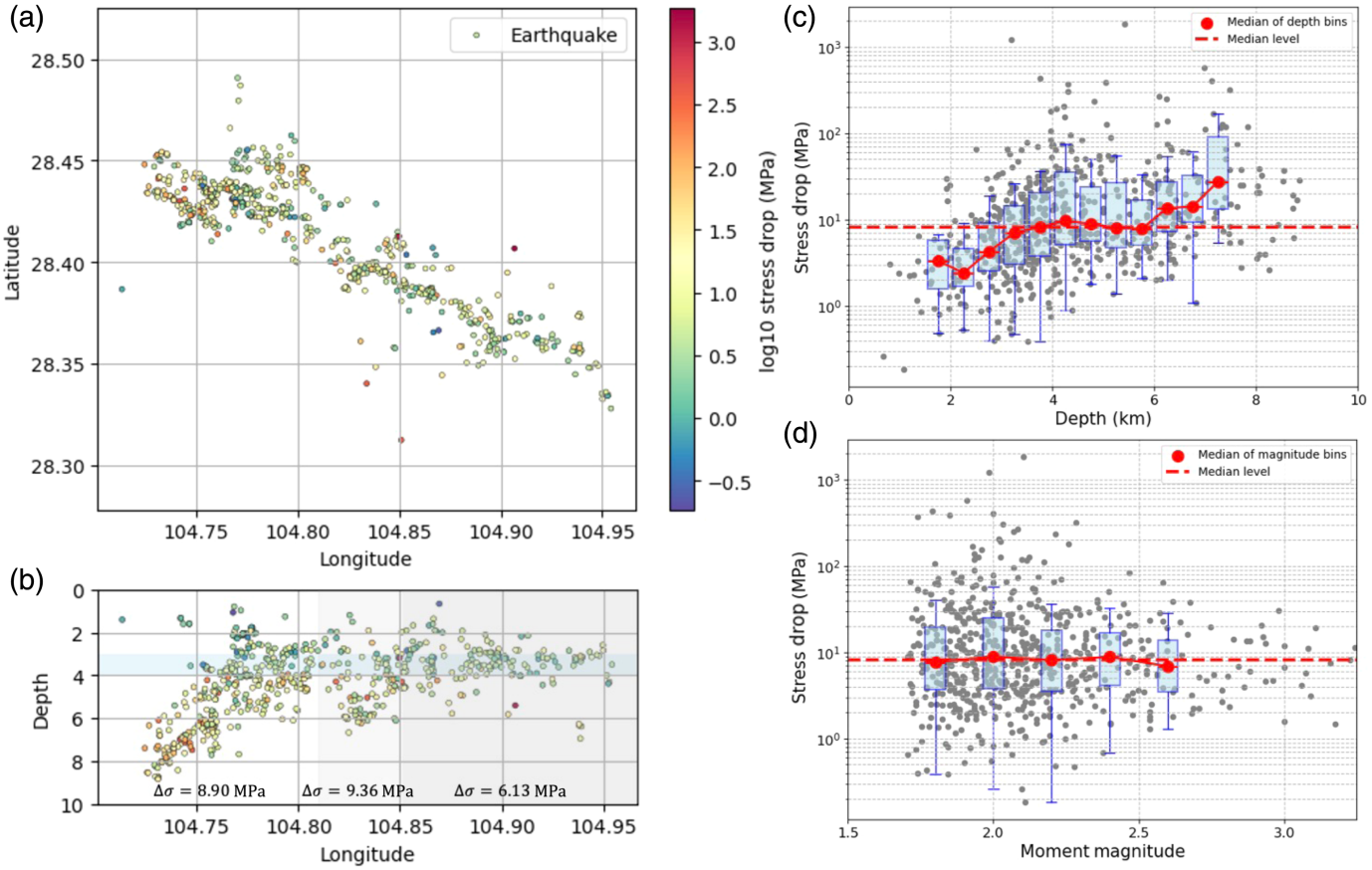


Figure 9. (a,c) Stress-drop estimates for M_L 1.0–4.0 earthquakes in the salt-mining region, Changning. Three sections of the Changning anticline fault system are shown by the same color as Figure 3c. The stress drops are the median value of each section, and the light-blue area shows the saltwater injection layer. (b, d) Stress-drop dependence on depth and magnitude, respectively. The blue dots represent the individual stress-drop values, and the red dots represent the median values in moment magnitude bins with an interval of 0.2, and depth bins with an interval of 0.5 km. It is required that in each bin there are at least 20 data points. The rectangle boxes represent the 25th (lower bar) and 75th (higher bar) percentiles of the values. The error bars extend from the box to the farthest data point lying within 1.5× the interquartile range from the box. The horizontal red-dashed lines indicate the median stress-drop levels in these cases. The color version of this figure is available only in the electronic edition.

the median corner frequency determined by the spectral ratio method. This could be understood that the spectral-decomposition-based method estimates a corner frequency for each event by averaging the spectra across all azimuths, which should approximate the median corner frequency of the same event from the spectral ratio method. However, if the directivity effect is observed for an event, then the corner frequency estimates accounting for the directivity effect should provide a more accurate observation for earthquake rupture processes than simply calculating a median corner frequency across different stations.

Although the stress-drop estimation of absolute values can be uncertain, the relative stress-drop measurements are much more reliable (Shearer *et al.*, 2019, 2024). Our analysis focuses on the results obtained from the spectral decomposition method within events for which $M_L > 1$ (Fig. S10). The analysis of depth and magnitude distributions (Figs. S6 and S11) shows a median aftershock depth of 4 km. A higher frequency of earthquakes occurs at depths of approximately 3–4 km and moment magnitudes of 1.8–2.0, particularly near the high pore pressure saltwater injection layer (~3 km; Yang *et al.*, 2024). The central section shows deeper seismicity (~5 km), potentially associated with a conjugate fault (Fig. 9b). The northwest section exhibits the deepest seismicity (5–8 km) with larger magnitudes along the east–west-trending anticlinal axis (Fig. S6d). The southeast section, situated near the mainshock and salt-mining injection wells, features lowest stress drop compared with the other two sections. The lower stress drops in the southeast section likely reflect regional stress relaxation and reduced stress accumulation resulting from long-term saltwater injection operations at relatively shallower depths over three decades, whereas the relatively higher stress drops in the northwest and central sections are more associated with generally deeper earthquakes distant from injection spots.

The minimized stress-drop scaling with moment magnitude (Fig. 9d) may indicate earthquake self-similarity within the three sections of the salt-mining area. The stress-drop scaling with depth (Fig. 9c) shows a significant increase in stress drop

Downloaded from http://pubs.geoscienceworld.org/ssa/srl/article-pdf/doi/10.1785/0220250172/7723274/srl-2025172.1.pdf by Chinese University Hong Kong user on 07 April 202

within the depth range of 2–4 km. The Cambrian to Silurian caprocks within this depth range (Fig. S3) are extensively fractured and faulted (Anyiam *et al.*, 2024). Influenced by saltwater injection, the high pore pressure in the target salt extraction formation reduces the effective normal stress, thereby facilitating slip on fractures and faults that might otherwise have remained stable. The prolonged injection unloads shear stress at the depth of ~3 km, resulting in lower stress drops and an increased frequency of earthquakes. It is challenging to apply reasonable corrections for depth-dependent attenuation and rupture velocity to eliminate the potential systematic dependence of stress drop on source depth within the upper 6 km of the salt-mining area. The wider depth range observed in the northwest section (Fig. S6a) primarily influences the stress-drop scaling with depth.

Heterogeneity of the Changning anticline

The primary rupture plane of the mainshock is a northwest–southeast-striking fault (strike 125°; Li *et al.*, 2020). However, the diversity of nodal plane orientations for the aftershock sequence, evidenced by the wide distribution of P-, T-, and B-axis orientations reveals significant complexity in fault geometry and stress patterns. Particularly, T-axis plunges are predominantly between 0° and 70° (Fig. 3b). Meanwhile, the resolved southeast rupture directivity (60° ± 10°) for several aftershocks is highly oblique to the mainshock's fault plane, indicating the activation of conjugate fault structures in the central anticline axis (Fig. 4). Dai *et al.* (2023) identified that on 23 June 2019, an M_w 4.3 aftershock that occurred near the identified conjugate fault was different from other $M_w > 4$ aftershocks. The M_w 4.3 event shows shear stress and high fluid overpressure, likely caused by the relatively large difference between the fault strike and the direction of the tectonic stress field for the mainshock.

The two M ~3 events exhibit notably slow rupture speeds ($V_r/V_S \sim 0.6$), approaching the lower bound of the typical patterns in which V_r/V_S ranges from 0.6 to 0.8 (Heaton, 1990) and notably slower than the average of 0.72 for moderate-to-large earthquakes (Geller, 1976). Although small earthquakes ($3.5 \le M \le 4.1$) with strong directivity typically show faster rupture velocities ($0.63V_S \le V_r \le 0.87V_S$), events with weak directivity propagate more slowly or bilaterally (Boatwright, 2007). The cosine relationship of azimuth-dependent corner frequencies demonstrates unilateral rupture directivity for the two target events. Smaller earthquakes are known to exhibit higher sensitivity to local geological conditions (Abercrombie *et al.*, 2017; Shelly, 2020; Huang *et al.*, 2025). Such slow rupture velocities likely result from a combination of fault geometry complexity and high pore pressure from prolonged salt-mining operations.

The 17 June 2019 M_s 6.0 Changning earthquake aftershocks provide a significant opportunity to investigate how a large mainshock interacts with a complex, pre-existing fault system under the influence of industrial activities. Our analysis of the aftershocks reveals that their rupture processes are not simple repetitions of the mainshock but instead map out a conjugate fault architecture and a locally perturbed stress field. The directivity observations for the central Changning fault section qualitatively agree with the focal mechanism patterns. Combined with the stress-drop variations, it can provide robust insights into fault interaction mechanisms. Despite over 30 yr of saltwater injection, most aftershocks show strike-slip faulting type, consistent with the regional stress patterns. It also suggests that induced seismicity following large earthquakes has lower seismic risks in our study area, unlike the more abrupt stress perturbations observed in hydraulic fracturing zones of the Changning region (Dai *et al.*, 2025). Therefore, analyzing source mechanisms and rupture directivities in these smaller events can help forecast regional fault systems, stress distribution, and the potential locations and characteristics of future induced earthquakes. These findings enhance our understanding of smaller induced seismicity processes and contribute to improved seismic hazard assessment in regions affected by energy production operations.

Conclusion

In this study, we first enhance the focal mechanism catalog of 857 earthquakes with $M_L > 1$ occurring in the salt-mining area of the Changning region from 6 July to 21 August 2019. Our high-resolution results show that the strike-slip rupturing of aftershocks in the Changning anticline is the primary faulting pattern, and the spatial diversity of nodal planes may result from fault geometry complexity or stress field heterogeneity at short-length scales. We focus on the middle segment of the Changning anticline and comprehensively estimate the rupture process of two induced earthquakes ($M_L \sim 3.0$) by applying the multiple EGF approach. It indicates northeastward rupture propagation (~60°) along a previously unidentified strike-slip conjugate fault at a relatively low-rupture velocity (~$0.6V_S$), contrasting with the northwestward rupture of the M_s 6.0 mainshock. Using the spectral decomposition method, we observe a spatial distribution of stress drop for three subsections in the Changning anticline. The stress drops are significantly increasing in the depth range of 2–4 km, which corresponds to the salt extraction layers. These findings contribute to our understanding of rupture processes across different earthquake magnitudes and highlight the importance of high-resolution seismic arrays in identifying source parameters of small-magnitude seismic events.

Data and Resources

Determination of pick polarities is conducted using the deep learning model PhaseNet+ (Zhu *et al.*, 2025; https://github.com/AI4EPS/EQNet), and the earthquake catalog is produced by Zhao, Zhang, *et al.* (2023; doi: 10.1016/j.tecto.2023.230086). The focal mechanism catalog is available from https://zenodo.org/records/15450041. Data processing largely depends on ObsPy (Beyreuther *et al.*, 2010;

Downloaded from http://pubs.geoscienceworld.org/ssa/srl/article-pdf/doi/10.1785/0220250172/7723274/srl-2025172.1.pdf by Chinese University Hong Kong user on 07 April 202

https://docs.obspy.org). Figures are made using PyGMT (https://www.pygmt.org) and Matplotlib (https://matplotlib.org). The National Earthquake Data Center is available at https://data.earthquake.cn. All websites were last accessed in July 2024. The supplemental material includes additional figures that provide more detailed insights into the results and discussion.

Declaration of Competing Interests

The author acknowledges that there are no conflicts of interest recorded.

Acknowledgments

Seismic waveform data were acquired by the Geophysical Exploration Center of China Earthquake Administration (CEA). This study was supported by the National Natural Science Foundation of China (Grant Number U2139203), Hong Kong Research Grant Council Grants (Grant Numbers 14308523 and 14306122), Shenzhen Fundamental Research Program (Shenzhen Natural Science Foundation, Grant Number JCYJ20250604141405007), 1+1+1 CUHK-CUHK(SZ)-GDSTC Joint Collaboration Fund, Faculty of Science and the Chinese University of Hong Kong (CUHK) Vice Chancellor's Ph.D. Scholarship Scheme.

References

Abercrombie, R. E. (2014). Stress drops of repeating earthquakes on the San Andreas Fault at Parkfield, *Geophys. Res. Lett.* **41,** 8784–8791.

Abercrombie, R. E. (2015). Investigating uncertainties in empirical Green's function analysis of earthquake source parameters, *J. Geophys. Res.: Solid Earth* **120,** 4263–4277.

Abercrombie, R. E., P. Poli, and S. Bannister (2017). Earthquake directivity, orientation, and stress drop within the subducting plate at the Hikurangi margin, New Zealand, *J. Geophys. Res.: Solid Earth* **122,** no. 12, 10,176–10,188.

Aki, K. (1967). Scaling law of seismic spectrum, *J. Geophys. Res.* **72,** no. 4, 1217–1231.

Allmann, B. P., and P. M. Shearer (2007). Spatial and temporal stress drop variations in small earthquakes near Parkfield, California, *J. Geophys. Res.: Solid Earth* **112,** no. B4, doi: 10.1029/2006JB004395.

Álvarez-Gómez, J. A. (2019). Fmc-earthquake focal mechanisms data management, cluster 2 and classification, *SoftwareX* **9,** 299–307.

Anyiam, U. O., J. Qian, Y. Tan, and H. Zhang (2024). Comprehensive seismic evidence for the inducing mechanism of extremely shallow 2019 Changning Ms 6.0 earthquake by solution salt mining, Sichuan basin, China, *Geology* **52,** no. 6, 441–446.

Anyiam, U. O., H. Zhang, Y. Tan, J. Qian, L. Gao, Y. Liu, K. Zuo, and C. Zhao (2023). Enhanced 3D velocity structure, seismicity relocation and basement characterization of Changning shale gas and salt mining regions in southern Sichuan basin, *Front. Earth Sci.* **10,** 1082122, doi: 10.3389/feart.2022.1082122.

Beyreuther, M., R. Barsch, L. Krischer, T. Megies, Y. Behr, and J. Wassermann (2010). ObsPy: A Python toolbox for seismology, *Seismol. Res. Lett.* **81,** no. 3, 530–533.

Boatwright, J. (1978). Detailed spectral analysis of two small New York state earthquakes, *Bull. Seismol. Soc. Am.* **68,** no. 4, 1117–1131.

Boatwright, J. (2007). The persistence of directivity in small earthquakes, *Bull. Seismol. Soc. Am.* **97,** no. 5, 1350–1362.

Boore, D. M., and W. B. Joyner (1978). The influence of rupture incoherence on seismic directivity, *Bull. Seismol. Soc. Am.* **68,** no. 2, 283–300.

Brune, J. N. (1970). Tectonic stress and the spectra of seismic shear waves from earthquakes, *J. Geophys. Res.* **75,** no. 26, 4997–5009.

Cesca, S., and S. Heimann (2011). Automated directivity analysis of acoustic emissions in a mine scale experiment, *Geophys. J. Int.* **184,** no. 2, 867–884.

Chen, H., X. He, H. Yang, and J. Zhang (2021). Fault-plane determination of the 4 January 2020 Offshore Pearl River Delta earthquake and its implication for seismic hazard assessment, *Seismol. Res. Lett.* **92,** 1913–1925.

Chu, S., A. Baltay, and R. Abercrombie (2024). Characterizing directivity in small (M 2.4–5) aftershocks of the Ridgecrest sequence, *Bull. Seismol. Soc. Am.* **115,** 1177–1188., doi: 10.1785/0120240146.

Dai, J., J. Liu, J. Yang, L. Wang, F. Xue, X. Shi, S. Dai, J. Hu, C. Liu, Y. Tang, and Y. Cai (2025). Statistical characteristics and causal mechanisms of hydraulic fracturing induced seismicity in the Southern Sichuan Basin, China, *J. Rock Mech. Geotech. Eng.* 1674–7755, doi: 10.1016/j.jrmge.2025.05.020.

Dai, K., Y. Zheng, R. Guo, and J. Xu (2023). Source characteristics of the mainshock and aftershocks of the 2019 Changning earthquake sequence: Implications for fluid effects, *Sci. China Earth Sci.* **66,** 1321–1333, doi: 10.1007/s11430-022-1040-4.

Ellsworth, W. L. (2013). Injection-induced earthquakes, *Science* **341,** 1225942, doi: 10.1126/science.1225942.

Folesky, J., J. Kummerow, S. A. Shapiro, M. Häring, and H. Asanuma (2016). Rupture directivity of fluid-induced microseismic events: Observations from an enhanced geothermal system, *J. Geophys. Res.: Solid Earth* **121,** no. 11, 8034–8047.

Geller, R. J. (1976). Scaling relations for earthquake source parameters and magnitudes, *Bull. Seismol. Soc. Am.* **66,** no. 5, 1501–1523.

Hanks, T. C., and H. Kanamori (1979). A moment magnitude scale, *J. Geophys. Res.* **84,** no. B5, 2348–2350.

Hardebeck, J. L., and P. M. Shearer (2002). A new method for determining first-motion focal mechanisms, *Bull. Seismol. Soc. Am.* **92,** 2264–2276, doi: 10.1785/0120010200.

Hardebeck, J. L., and P. M. Shearer (2003). Using S/P amplitude ratios to constrain the focal mechanisms of small earthquakes, *Bull. Seismol. Soc. Am.* **93,** no. 6, 2434–2444.

Heaton, T. H. (1990). Evidence for and implications of self-healing pulses of slip in earthquake rupture, *Phys. Earth Planet. In.* **64,** no. 1, 1–20.

Holmgren, J. M., G. M. Atkinson, and H. Ghofrani (2019). Stress drops and directivity of induced earthquakes in the Western Canada Sedimentary Basin, *Bull. Seismol. Soc. Am.* **109,** 1635–1652, doi: 10.1785/0120190035.

Huang, C., W. Xu, R. Bürgmann, L. Xie, G. Feng, B. Shan, Z. Li, Y. Aoki, Y. Zhang, J. Zhu, *et al.* (2025). Heterogeneous strong asperities and tectonic complexity control irregular cascading ruptures, *Sci. Adv.* **11,** eadv6771, doi: 10.1126/sciadv.adv6771.

Huang, Y., G. C. Beroza, and W. L. Ellsworth (2016). Stress drop estimates of potentially induced earthquakes in the Guy-Greenbrier sequence, *J. Geophys. Res.: Solid Earth* **121,** no. 9, 6597–6607.

Jia, D., G. Wei, Z. Chen, B. Li, Q. Zeng, and G. Yang (2006). Longmen Shan fold-thrust belt and its relation to the western Sichuan Basin in

Downloaded from http://pubs.geoscienceworld.org/ssa/srl/article-pdf/doi/10.1785/0220250172/7723274/srl-2025172.1.pdf by Chinese University Hong Kong user on 07 April 202

central China: New insights from hydrocarbon exploration, *Am. Assoc. Petrol. Geol. Bull.* **90,** 1425–1447, doi: 10.1306/03230605076.

Jia, Z., P. M. Shearer, and W. Fan (2025). Rupture directivity from energy envelope deconvolution: Theory and application to 69 Ridgecrest M 3.5–5.5 earthquakes, *Earth Arxiv*, doi: 10.31223/X54M7H.

Kaneko, Y., and P. M. Shearer (2015). Variability of seismic source spectra, estimated stress drop, and radiated energy derived from cohesive-zone models of symmetrical and asymmetrical circular and elliptical ruptures, *J. Geophys. Res.: Solid Earth* **119,** no. 2, 1053–1079.

Király-Proag, E., C. Satriano, P. Bernard, and S. Wiemer (2019). Rupture process of the M 3.3 earthquake in the St. Gallen 2013 geothermal reservoir, Switzerland, *Geophys. Res. Lett.* **46,** no. 14, 7990–7999.

Kisslinger, C. (1980). Evaluation of S to P amplitude rations for determining focal mechanisms from regional network observations, *Bull. Seismol. Soc. Am.* **70,** no. 4, 999–1014.

Lei, X., D. Huang, J. Su, G. Jiang, X. Wang, H. Wang, X. Guo, and H. Fu (2018). Fault reactivation and earthquakes with magnitudes of up to Mw 4.7 induced by shale gas hydraulic fracturing in Sichuan basin, China, *Rev. Geophys. Planet. Phys.* **49,** no. 6, 566–581.

Lei, X., S. Ma, W. Chen, C. Pang, J. Zeng, and B. Jiang (2013). A detailed view of the injection-induced seismicity in a natural gas reservoir in Zigong, southwestern Sichuan Basin, China, *J. Geophys. Res. Solid Earth* **118,** 4296–4311, doi: 10.1002/jgrb.50310.

Lei, X., Z. Wang, and J. Su (2019). Possible link between long-term and short-term water injections and earthquakes in salt mine and shale gas site in Changning, south Sichuan Basin, China, *Earth Planet. Phys.* **3,** 510–525, doi: 10.26464/epp2019052.

Li, J., J. Xu, H. Zhang, W. Yang, Y. Tan, F. Zhang, L. Meng, Y. Zang, S. Miao, C. Guo, *et al.* (2023). High seismic velocity structures control moderate to strong induced earthquake behaviors by shale gas development, *Comm. Earth Environ.* **4,** doi: 10.1038/s43247-023-00854-x'.

Li, W., S. Ni, C. Zang, and R. Chu (2020). Rupture directivity of the 2019 Mw 5.8 Changning, Sichuan, China, earthquake and implication for induced seismicity, *Bull. Seismol. Soc. Am.* **110,** no. 5, 2138–2153.

Lin, M., Q. Li, W. Chen, G. Liu, D. Z. Wang, L. J. Zhao, T. C. Sheng, W. L. Zhou, L. Y. Wang, Z. S. Nie, *et al.* (2025). High-rate GNSS-based rapid determination of coseismic deformation and source characteristics for the 2023 M6.2 Jishishan earthquake, *Earthq. Sci.* **38,** no. 3, 187–200, doi: 10.1016/j.eqs.2025.01.002.

Liu, J., and J. Zahradník (2020). The 2019 Mw 5.7 Changning earthquake, Sichuan basin, China: A shallow doublet with different faulting styles, *Geophys. Res. Lett.* **47,** no. 4, 2019GL085408, doi: 10.1029/2019GL085408.

Liu, Q., M. Zhou, X. Tian, Y. Qiu, Z. Shen, Q. Wang, and C. Wang (2023). High‐resolution shear‐wave velocity structure of the 2019 6.0 Changning earthquake region and its implication for induced seismicity, *Seismol. Res. Lett.* **94,** 1392–1404, doi: 10.1785/0220220253.

Liu, R., D. Jiang, J. Zheng, F. Hao, C. Jing, H. Liu, J. Zhang, and G. Wei (2021). Stress heterogeneity in the Changning shale-gas field, southern Sichuan basin: Implications for a hydraulic fracturing strategy, *Mar. Petrol. Geol.* **132,** 105218, doi: 10.1016/j.marpetgeo.2021.105218.

López-Comino, J., and S. Cesca (2018). Automated full moment tensor inversion of coal mining induced seismicity, *Geophys. J. Int.* **212,** no. 2, 1247–1263.

Ni, S., H. Kanamori, and D. Helmberger (2005). Energy radiation from the Sumatra earthquake, *Nature* **434,** 582, doi: 10.1038/434582a.

Shearer, P. M., R. E. Abercrombie, D. T. Trugman, and W. Wang (2019). Comparing EGF methods for estimating corner frequency and stress drop from P wave spectra, *J. Geophys. Res.: Solid Earth* **124,** 3966–3986, doi: 10.1029/2018JB016957.

Shearer, P. M., G. A. Prieto, and E. Hauksson (2006). Comprehensive analysis of earthquake source spectra in southern California, *J. Geophys. Res.: Solid Earth* **111,** no. B6, doi: 10.1029/2005JB003979.

Shearer, P. M., I. Vandevert, W. Fan, R. E. Abercrombie, D. Bindi, G. Calderoni, X. Chen, W. Ellsworth, R. Harrington, Y. Huang, *et al.* (2024). Earthquake source spectra estimates vary widely for two Ridgecrest aftershocks because of differences in attenuation corrections, *Bull. Seismol. Soc. Am.* **115,** 777–791, doi: 10.1785/0120240134.

Shelly, D. R. (2020). A high-resolution seismic catalog for the initial 2019 Ridgecrest earthquake sequence: Foreshocks, aftershocks, and faulting complexity, *Seismol. Res. Lett.* **91,** no. 4, 1971–1978.

Skoumal, R. J., J. L. Hardebeck, and P. M. Shearer (2024). Skhash: A python package for computing earthquake focal mechanisms, *Seismol. Res. Lett.* **95,** doi: 10.1785/0220230329.

Sokos, E. N., and J. Zahradník (2008). ISOLA a Fortran code and a MATLAB GUI to perform multiple-point source inversion of seismic data, *Comput. Geosci.* **34,** no. 8, 967–977.

Somerville, P. G., N. F. Smith, R. W. Graves, and N. A. Abrahamson (1997). Modification of empirical strong ground motion attenuation relations to include the amplitude and duration effects of rupture directivity, *Seismol. Res. Lett.* **68,** no. 1, 199–222.

Song, J., W. Zhu, J. Zi, H. Yang, and R. Chu (2025). An enhanced focal mechanism catalog of induced earthquakes in Weiyuan, Sichuan, from dense array data and a multitask deep learning model, *Seism. Record* **5,** no. 2, 175–184.

Storn, R., and K. Price (1997). Differential evolution—A simple and efficient heuristic for global optimization over continuous spaces, *J. Global Optim.* **11,** 341–359.

Sun, X., P. Yang, and Z. Zhang (2017). A study of earthquakes induced by water injection in the Changning salt mine area, SW China, *J. Asian Earth Sci.* **136,** 102–109, doi: 10.1016/j.jseaes.2017.01.030.

Tan, Y., and D. Helmberger (2010). Rupture directivity characteristics of the 2003 Big Bear sequence, *Bull. Seismol. Soc. Am.* **100,** no. 3, 1089–1106.

Tang, X., R. Guo, Y. Zhang, K. Dai, J. Xu, J. Zhou, M. Hou, and H. Sun (2024). Rapid rupture characterization for the 2023 Ms 6.2 Jishishan earthquake, *Earthq. Res. Adv.* **4,** no. 2, 100288, doi: 10.1016/j.eqrea.2024.100288.

Trugman, D. T., S. X. Chu, and V. C. Tsai (2021). Earthquake source complexity controls the frequency dependence of near-source radiation patterns, *Geophys. Res. Lett.* **48,** doi: 10.1029/2021GL095022.

Vandevert, I. C., P. M. Shearer, and W. Fan (2024). Ridgecrest aftershock stress drops from P- and S-wave spectral decomposition, *Bull. Seismol. Soc. Am.* **115,** 792–804, doi: 10.1785/0120240133.

Warren, L. M., and P. M. Shearer (2006). Systematic determination of earthquake rupture directivity and fault planes from analysis of long-period P-wave spectra, *Geophys. J. Int.* **164,** no. 1, 46–62.

Downloaded from http://pubs.geoscienceworld.org/ssa/srl/article-pdf/doi/10.1785/0220250172/7723274/srl-2025172.1.pdf by Chinese University Hong Kong user on 07 April 202

Yang, H., R. Guo, G. Zhai, J. Zhou, K. Dai, Y. Zheng, L. Li, and H. Sun (2024). Induced seismicity in the Changning salt mining zone, China, could be driven by the pore-pressure diffusion, *Tectonophysics* **871,** 230197, doi: 10.1016/j.tecto.2023.230197.

Yang, H., Y. Liu, M. Wei, J. Zhuang, and S. Zhou (2017). Induced earthquakes in the development of unconventional energy resources, *Sci. China Earth Sci.* **60,** 1–13.

Yang, H., D. Wang, R. M. Guo, M. Y. Xie, Y. Zang, Y. Wang, Q. Yao, C. Cheng, Y. R. An, and Y. Y. Zhang (2022). Rapid report of the 8 January 2022 MS 6.9 Menyuan earthquake, Qinghai, China, *Earthq. Res. Adv.* **2,** no. 1, doi: 10.1016/j.eqrea.2022.100113.

Yang, H., P. Zhou, N. Fang, G. Zhu, W. Xu, J. Su, F. Meng, and R. Chu (2020). A shallow shock: The 25 February 2019 ML 4.9 earthquake in the Weiyuan shale gas field in Sichuan, China, *Seismol. Res. Lett.* **91,** no. 6, 3182–3194.

Yang, W., E. Hauksson, and P. M. Shearer (2012). Computing a large refined catalog of focal mechanisms for southern California (1981–2010): Temporal stability of the style of faulting, *Bull. Seismol. Soc. Am.* **102,** no. 3, 1179–1194.

Yao, S., Z. Yang, and H. Yang (2025). Determination of rupture directivity of the 2024 Feidong M 4.7 earthquake using single near-source station, *Earthq. Sci.* **38,** 1–9.

Yi, G., F. Long, M. Liang, M. Zhao, and S. Wang (2020). Geometry and tectonic deformation of seismogenic structures in the Rongxian-Weiyuan-Zizhong region, Sichuan basin: Insights from focal mechanism solutions, *Chin. J. Geophys.* **63,** 3275–3291, doi: 10.6038/cjg2020O0095.

Yu, H., H. Kao, B. Wang, and R. Visser (2022). Long?term fluid injection can expedite fault reactivation and development: Riedel Shear structures illuminated by induced earthquakes in Alberta, Canada, *J. Geophys. Res.: Solid Earth* **127,** e2022JB025126, doi: 10.1029/2022JB025126.

Zhang, J., X. Chen, and R. E. Abercrombie (2022). Spatiotemporal variability of earthquake source parameters at Parkfield, California, and their relationship with the 2004 M6 earthquake, *J. Geophys. Res.: Solid Earth* **127,** doi: 10.1029/2021JB022851.

Zhang, J., and H. Yang (2025). Improved source parameter estimation of earthquakes in the 2019 Ridgecrest Sequence based on a global-optimization algorithm and their implications on fault behaviors, *Bull. Seismol. Soc. Am.* doi: 10.1785/0120240111.

Zhang, J., H. Yang, J. Zi, J. Su, and X. Chen (2024). An improved estimation of stress drop and its application on induced earthquakes in the Weiyuan shale gas field in China, *Geophys. J. Int.* **236,** no. 3, 1785–1803.

Zhang, Y., Y. An, F. Long, G. Zhu, M. Qin, Y. Zhong, Q. Xu, and H. Yang (2021). Short-term foreshock and aftershock patterns of the 2021 Ms 6.4 Yangbi earthquake sequence, *Seismol. Res. Lett.* **93,** no. 1, 21–32.

Zhang, Z., C. Liang, F. Long, M. Zhao, and D. Wang (2022). Spatiotemporal variations of focal mechanism solutions and stress field of the 2019 Changning Ms 6.0 earthquake sequence, *Front. Earth Sci.* **9,** 79790, doi: 10.3389/feart.2021.797907.

Zhao, Y., G. Jiang, X. Lei, C. Xu, B. Zhao, and X. Qiao (2023). The 2021 Ms 6.0 Luxian (China) earthquake: Blind reverse-fault rupture in deep sedimentary formations likely induced by pressure perturbation from hydraulic fracturing, *Geophys. Res. Lett.* **50,** no. 7, e2023GL103209, doi: 10.1029/2023GL103209.

Zhao, Y., M. Zhang, Y. Duan, X. Lei, and Q. Liu (2023). Seismogenic structures and earthquake mechanisms in the Changning area, China: Insights from seismicity and tomography, *Tectonophysics* **869,** 230086, doi: 10.1016/j.tecto.2023.230086.

Zhu, L., and D. V. Helmberger (1996). Advancement in source estimation techniques using broadband regional seismograms, *Bull. Seismol. Soc. Am.* **86,** no. 5, 1634–1641.

Zhu, W., and G. C. Beroza (2019). Phasenet: A deep-neural-network-based seismic arrival-time picking method, *Geophys. J. Int.* **216,** no. 1, 261–273.

Zhu, W., J. Song, H. Wang, and J. Münchmeyer (2025). Phasenet+: End-to-end earthquake monitoring using a multitask deep learning model, doi: 10.48550/arXiv.2506.06939.

Zi, J., H. Yang, J. Su, and L. Chen (2023). Structural constraints of induced earthquakes in the Weiyuan Shale Gas Field revealed by high-resolution body-wave tomography and earthquake relocation, *Tectonophysics* **864,** doi: 10.1016/j.tecto.2023.230007.

Zi, J., Y. Yang, H. Yang, and J. Su (2025). The 11-month precursory fault activation of the 2019 ML 5.6 earthquake in the Weiyuan shale gas field, China, *Comm. Earth Environ.* **6,** doi: 10.1038/s43247-025-02151-1.

Zuo, K., C. Zhao, and H. Zhang (2020). 3D crustal structure and seismicity characteristics of Changning–Xingwen area in the southwestern Sichuan Basin, China, *Bull. Seismol. Soc. Am.* **110,** 2154–2167, doi: 10.1785/0120200085.

Manuscript received 21 May 2025
Published online 12 January 2026

Downloaded from http://pubs.geoscienceworld.org/ssa/srl/article-pdf/doi/10.1785/0220250172/7723274/srl-2025172.1.pdf by Chinese University Hong Kong user on 07 April 202